Coupled CFD/CSD Computation of Airloads of an Active Twist Rotor

Steven J. Massey[*] and Andrew R. Kreshock,[†]
and Martin K. Sekula[‡]

NASA Langley Research Center, Hampton, VA 23681-2199

An unsteady Reynolds averaged Navier-Stokes analysis loosely coupled with a comprehensive rotorcraft code for blade trim and aeroelastic effects is presented for a second-generation Active Twist Rotor. High fidelity Navier-Stokes results are compared to lifting-line theory based comprehensive rotorcraft code calculations and wind tunnel data. Results indicate that the CFD/CSD solutions are mesh converged and in very good agreement with flapwise bending moments for both the low and high advance ratio cases presented. The accuracy of the predicted rotor torque is also very good across the full sweep of advance ratio cases available for comparison with data.

Nomenclature

Symbols

μ	advance ratio
M	Mach number
M_β	flapwise bending moment, in-lb
M_θ	torsional bending moment, in-lb
M_ξ	chordwise bending moment, in-lb
R	normalized rotor radius
ψ	azimuthal coordinate, deg
y^+	dimensionless, sublayer-scaled wall coordinate of first node away from surface

Acronyms

ARES	Aeroelastic Rotor Experimental System
ATR	Active Twist Rotor
CAD	Computer-Aided Design
CAMRAD	Comprehensive Analytical Model of Rotorcraft Aerodynamics and Dynamics
CFD	Computational Fluid Dynamics
CSD	Computational Structural Dynamics
DiRTlib	Donor interpolation Receptor Transaction library
MFC	Macro-Fiber Composite
SUGGAR	Structured, Unstructured, and Generalized overset Grid AssembleR

---

[*]Research Aerospace Engineer, Aeroelasticity Branch, MS 340, Senior Member AIAA
[†]Research Aerospace Engineer, U.S. Army Research Laboratory, Vehicle Technology Directorate, MS 340
[‡]Aerospace Engineer, Aeroelasticity Branch, MS 340

I.   Introduction

AN unsteady Reynolds averaged Navier-Stokes analysis coupled with a comprehensive rotorcraft code for blade trim and aeroelastic effects is presented for a second-generation Active Twist Rotor (ATR) with fuselage, Figure 1. Active-twist control has been studied for the past decade as a means of higher harmonic control and individual blade control. The ATR concept has been studied, both numerically[1,2] and experimentally,[3] as a method to reduce vibratory loads, reduce rotor system noise, and improve performance. ATR blades generate dynamic twist during rotor operation by means of piezoelectric composite actuators embedded in the skin of the blade, Figure 2. The piezoelectric fibers are oriented at $\pm 45°$ from the blade span, and thus generate shear strains in the skin that induce twist in the blade. The first generation of NASA/Army/MIT ATR blades used Active Fiber Composite (AFC) actuators, and were tested at the Transonic Dynamics Tunnel at NASA Langley Research Center.[4] The ATR blades demonstrated sufficient twist authority to be able to minimize the primary vibratory loads induced by the rotor during flight. A set of second-generation active-twist rotor blades have been manufactured that provide greater control authority so that investigation can be conducted on simultaneous application of multiple ATR objectives, such as, vibratory load reduction, noise reduction and blade tracking. The ATR blades use macro-fiber composite (MFC) piezoelectric actuators, which have more control authority than the AFC actuators. MFC actuators were originally developed at NASA Langley Research Center,[5] and have since been transitioned into a commercial product. Since the objective of the first generation ATR blades was demonstration of concept, minimal amount of effort was expended to optimize the performance of the blades and create accurate predictions of the active response. Later work by Cesnik et al[6] and continued by Thornburgh et al[7] has used more detailed modeling methods to optimize the structural response of ATR blades and predict the beam properties. The tools created by Cesnik and modified by Thornburgh create a baseline linear model that has been validated against blade performance. Additional comprehensive beam analysis using CAMRAD II[8] and the results from the University of Michigan/Variational Asymptotic Beam Sectional (UM-VABS)[9,10] analysis permit accurate prediction of the frequency response of the ATR blade during both bench testing and rotor operation. This structural model in CAMRAD II can then be coupled with CFD analysis using FUN3D.[11,12] This coupling allows for a high fidelity structural and aerodynamic model that can be validated by wind-tunnel testing. Experimental data used for the validation of the coupled CFD/CSD model of the ATR in this study were obtained from a recent wind tunnel test[13] in NASA Langley's Transonic Dynamics Tunnel.

II.   Computational Methodology

A.   CFD Mesh Generation

Meshes of coarse, medium, and fine levels of refinement were constructed following the general design and mesh spacing based on the best practices published by Biedron and Lee-Rausch.[14] One departure from their original template was the doubling of the farfield boundary extent to ten rotor radii, which is part of their updated best practices. The rotor blade mesh was constructed using the same CAD definition used in the construction of the wind tunnel test blades. The fuselage was modeled based on the current configuration of the Aeroelastic Rotor Experimental System (ARES)[15] test bed. A surface definition of the ARES and ATR blades is presented in Figure 3. A non-rotating mast, shaded in blue, was added to the fuselage as a first attempt at modeling the rotating mast and hub cover, compare Figures 1 and 3. Unstructured tetrahedral meshes were generated using VGRID[16] with input prepared using GridTool.[17] Tetrahedra in the boundary layer were merged into prisms using a utility program included in the FUN3D suite. The boundary layer was fully meshed with a first cell height of 1.09×10^{-5} inches on the blade corresponding to $y^+ < 1.0$ and 3.43×10^{-5} inches for the fuselage, which gives a $y^+ \approx 1.0$ nearly everywhere, Figure 4. Node counts for the coarse, medium, and fine meshes are 7.2, 17.7, and 53.5 million nodes, respectively, with the blades accounting for about three-quarters of the nodes in each mesh. In Figure 5, the surface mesh is shown in black with a cut down the middle of the domain shown in blue for the medium mesh.

B.   CFD Solver

Solutions to the Reynolds averaged Navier-Stokes (RANS) equations are computed using the FUN3D[11,12] flow solver. Details of the FUN3D features employed for rotorcraft simulations are given by Biedron and Lee-Rausch.[18] For this study, turbulence closure is obtained using the Spalart-Allmaras[19] one-equation model. Inviscid fluxes are computed using the Roe scheme.[20] For second-order spatial accuracy the convective fluxes are computed using a least-squares technique. In high gradient regions of the flow, limiters on these reconstructed values may be needed for stability. However, in the present computations, no limiters were required. Time integration is accomplished by an Euler

American Institute of Aeronautics and Astronautics

implicit backwards difference scheme with dual time stepping to achieve second-order accuracy.[21, 22] Following best practices, all solutions were generated using 25 subiterations in the present study. Early numerical experiments showed this number of subiterations was more than enough to achieve subiteration convergence. Mesh motion due to blade deformations is carried out by treating the CFD mesh as a linear elastic medium with material properties based on the mesh characteristics with appropriate application of the Geometric Conservation Law.[23] Rotor motion is handled by means of an overset mesh methodology which is implemented in FUN3D via the Donor interpolation Receptor Transaction library (DiRTlib)[24] and the Structured, Unstructured, and Generalized overset Grid AssembleR (SUGGAR).[25]

C. CSD Solver

The present study employed the second generation version of the Comprehensive Analytical Model of Rotorcraft Aerodynamics and Dynamics (CAMRAD II)[8] to predict the dynamic behavior of the ATR rotor. CAMRAD II is a rotorcraft-centric aeromechanical analysis tool that combines a multibody dynamics formulation with nonlinear finite elements to model rotorcraft structures: rotors, control systems, fuselage, and various aerodynamic surfaces. CAMRAD II incorporates a lifting line model (with or without a table lookup) to determine the rotor aerodynamic loads, with a customizable wake model ranging in complexity from a simple linear inflow to a deforming free wake. Because the aerodynamic models within CAMRAD II are based on lifting-line theory coupled with airfoil tables and wake models, higher fidelity Navier-Stokes aerodynamics are imported into CAMRAD II via a loose coupling procedure first suggested by Tung et al[26] and implemented in FUN3D by Biedron and Lee-Rausch.[18] In the present study, airloads data from the CFD solver and blade motion data from the CFD solver are exchanged at periodic intervals of twice per revolution.

D. CFD/CSD Coupling Details

The loads from the CFD grid are transferred to the CSD code through an intermediate code. The CFD code calculates the sectional loads along the blade. The intermediary code takes the differential load between the CFD and the CSD solvers and interpolates it to locations that correspond with the CSD aerodynamic panels. A new differential load is then applied to the CSD model for every coupling cycle until convergence is established. Convergence was typically monitored by the control angles, rotor thrust and torque. To complete the coupling cycle after the CSD code has trimmed to a new solution, the motion differential, due to the updated loads, is transferred back to the CFD code which then generates new motion and grid deformations.

E. CAMRAD II Rotor Model

The ATR rotor is a 4-bladed, articulated, 10.56 foot diameter rotor, with a blade planform representative of an attack-class helicopter. The rotor has a solidity of 0.0928 and includes a 20°swept tip in the outer seven percent of the rotor radius. The structural model of the rotor consists of three radial sections: (1) rigid hub, (2) rigid section of the blade and cuff, and (3) elastic blade. The inboard-most section represents the rotor hub and is approximated by a rigid beam element. The two sections outboard of the hub represent the rotor blades. The inner section is modeled by three rigid elements representing (1) the structure between the flap-lag hinges and blade pitch bearing, (2) the blade cuff, and (3) the inboard section of the actual rotor blade which is made of solid fiberglass to provide a reliable interface with the cuff. Mass and inertial properties of these inboard elements were determined by experiment and CAD analysis. The outboard most section, representing the outer 87% of the rotor blade, consists of eleven elastic beam elements. Each beam element has elastic flap, lag, torsion, and extension degrees of freedom. Structural properties of these beam elements were determined through analysis of the blade layup using UM-VABS software. The fidelity of the blade structural model was confirmed through bench testing of each blade to determine their natural frequencies and deflections due to applied loads.

Two of CAMRAD II's internal aerodynamic models are employed in this analysis. First is a free wake model. This model represents the blade aerodynamic loads through a 25-panel lifting line model. The deformable, single peak wake extends two rotor revolutions from the rotor blades. The second internal aerodynamic model is a uniform inflow model with a 96-panel lifting line model employed for coupling with the CFD solver, which exports its aerodynamics at 200 radial stations along the blade. The aerodynamic and structural models result in a large number of equations of motion therefore a modal reduction, using 10 blade modes, is used to reduce the number of degrees of freedom in the model. The resulting blade equations of motion are solved using a harmonic balance method. The four rotor blades are assumed to be identical, therefore the equations of motion are solved for a single blade. The phase of the solution is adjusted for each rotor blade, and the loads of all the blades are summed to produce the rotor loads.

American Institute of Aeronautics and Astronautics

Rotor trim is determined by a Newton-Raphson approach. The control inputs are the rotor collective pitch, lateral cyclic pitch, and longitudinal cyclic pitch which are used to eliminate 1/rev blade flapping while providing a specified rotor thrust. The rotor shaft tilt is specified to match experimental shaft tilt, instead of being included as a variable in the trim solution. This approach was applied to both the free wake and the coupled CFD/CSD solution for consistency, since the methodology behind the CFD/CSD solution requires the rotor shaft angle to remain constant.

III.   Results and Discussion

The goal of this paper is to establish a baseline for coupling FUN3D/CAMRAD II without active controls and compare the results to experimental values. The runs were conducted over an advance ratio sweep of 0.13 to 0.33. To characterize mesh convergence, the extremities of the sweep was computed with two additional levels of mesh refinement. The computed total rotor torque for the sweep is seen to be in good agreement with measurements, see Figure 6. The coarse grid is within 10% of the measured value for the entire advance ratio sweep, however, mesh renement shows a trend of an increasing under prediction of torque. Also plotted is the CAMRAD II free wake model results without coupling to FUN3D. The CFD/CSD coupling provides better agreement with measurements than the free wake model. For brevity, detailed results will only be provided for the lowest and highest advance ratios in the sweep.

For each run two revolutions were solved before the first coupling cycle to insure the flow field was established, then six trim cycles were performed, with CFD/CSD coupling occurring at a frequency of twice per rotor revolution. Trim convergence was established by monitoring the pitch hinge angle change (less than 0.01°after six cycles) as well as the percent differences between FUN3D and CAMRAD II predictions of thrust and torque which were on the order of than 0.04% and 0.1% respectively after six cycles. Plots of flapwise, torsional and chordwise bending moments (mean removed) at three radial stations on the fine mesh demonstrate that the computed airloads are converged by the fifth coupling cycle, Figures 7 and 8. For reference, measured values averaged over multiple revolutions with the mean removed and error bars of plus or minus one standard are deviation included on the trim bending moment convergence plots. The radial stations were chosen based on available sensor data and where the largest range was observed in the plotted quantities. Though not plotted, coarse and medium meshes exhibited the same trim convergence behavior.

Mesh convergence can be seen to be very good for computed airloads at these same three radial stations, as shown in Figures 9 and 10. Given the very small differences between meshes, the coarse grid is deemed to be sufficiently accurate. Though each of the quantities show the same level of mesh convergence, the flapwise moments are seen to be in the best agreement with data for both advance ratios shown. Also, the CAMRAD II free wake model is seen to perform well for the low advance ratio case, while performing significantly worse than the coupled CFD/CSD computations for the higher advance ratio case shown in Figure 10. It is important to note that the phase of the first quadrant of each of the flapwise peaks has improved drastically compared to the CAMRAD II model, with slight improvement with the fine mesh over the coarse mesh.

Wind tunnel measurements of flapwise bending moment at 8 stations on each rotor blade for minimum and maximum advance ratios are presented in Figures 11 and 12. The reduced contour radii for blades 1 and 2 are indicative of the lack of tip sensor data. Minor blade-to-blade variation in the data is visible and is reflected in the mean and standard deviation computations shown in previous line plots. It should be noted that the maximum and minimum flapwise bending moments measured on blade 3 exhibit a larger range than the other three blades. Since blade 4 has the most extensive set of measured blade moment data and the inboard measurements best match blade 1 and 2 measurements, its measurements will be plotted alongside computed values in Figures 13 and 14. For the low advance ratio case, shown in Figure 13, the CAMRAD II free wake model provides the best prediction of the maximum and minimum values of flapwise bending moment measured on blade 4 at azimuth angles of 290°and 345°respectively. The CFD/CSD results at the same azimuth angles more closely match the out-of-family moments measured on blade 3, Figure 11(c), than blade 4 moments. Refinements in the grid mesh appear to further improve correlation with blade 3 data. Figure 14 presents a comparison of the measured flapwise bending moment on blade 4 to moments computed using the CAMRAD II free wake model and the various CFD/CSD models. The free wake model significantly under predicts the amplitudes of the bending moment extreme while the three CFD/CSD solutions over predict the radial and azimuthal extent of the high flapwise bending moment regions which occur at approximately 190°and 270°.

Similar sets of contour plots of the rotor disk for torsional and chordwise moments are presented in Figures 15 through 18. These plots do not include wind tunnel data due to the lack of sensor data, but the same trends identified in the previous plots are still evident, namely, CAMRAD II free wake model is comparable to CFD/CSD for the low advance ratio case, while significantly different for the higher advance ratio case.

American Institute of Aeronautics and Astronautics

IV. Concluding Remarks

An unsteady Reynolds averaged Navier-Stokes solver (FUN3D) loosely coupled with a comprehensive rotorcraft code (CAMRAD II) for blade trim and aeroelastic effects was presented for a second-generation Active Twist Rotor. Results indicate that the CFD/CSD solutions were mesh and trim converged and in very good agreement with flapwise bending moments for both the low and high advance ratio cases presented. The predicted rotor torque was also in very good agreement with data across the full sweep of advance ratio cases available. CAMRAD II free wake solutions were seen to provide better moment predictions at low advance ratio conditions, though computations of torque was not indicative of the departure from data seen in the flapwise, torsional and chordwise bending moment results. Future computations will build on the present validation results to include active twist control.

Acknowledgments

References

[1]Booth, E. R. and Wilbur, M. L., "Acoustic Aspects of Active-Twist Rotor Control," *Journal of the American Helicopter Society*, Vol. 49, No. 1, Jan. 2004, pp. 3–10.

[2]Fogarty, D. E., Wilbur, M. L., and Sekula, M. K., "A Computational Study of BVI Noise Reduction Using Active Twist Control," *American Helicopter Society 66th Annual Forum Proceedings*, Phoenix,AZ, May 2010.

[3]Bernhard, A. P. F. and Wong, J., "Wind-Tunnel Evaluation of a Sikorsky Active Rotor Controller Implemented on the NASA/Army/MIT Active Twist Rotor," *American Helicopter Society 59th Annual Forum Proceedings*, Phoenix,AZ, May 2003.

[4]Wilbur, M. L., Mirick, P. H., Yeager, W. T., Langston, C. W., Cesnick, C. E. S., and Shin, S., "Vibratory Loads Reduction Testing of the NASA/Army/MIT Active Twist Rotor," *American Helicopter Society 57th Annual Forum Proceedings*, Washington, DC, May 2001.

[5]Wilkie, W. K., Bryant, R. G., High, J. W., Fox, R. L., Ileilbaum, R. F., Jalink, A., Little, B. D., and Mirick, P. H., "Low-Cost Piezocomposite Actuator for Structural Control Applications," *SPIE 7th Annual International Symposium on Smart Structures and Materials*, Newport Beach, CA, 2000.

[6]Cesnik, C., Mok, J., Morillo, J., and Parikh, A., "Design Optimization of Active Twist Rotor Blades," *European Rotorcraft Forum*, Ann Arbor, MI, 2004.

[7]Thornburgh, R., Kreshock, A., and Wilbur, M., "Structural Optimization of Active-Twist Rotor Blades," *American Helicopter Society 67th Annual Forum Proceedings*, Virginia Beach, VA, 2011.

[8]Johnson Aeronautics, Palo Alto, CA, *Comprehensive Analytical Model of Rotorcraft Aerodynamics and Dynamics II v4.6*, 2007.

[9]Cesnik, C. E. S. and Hodges, D. H., "VABS: A New Concept for Composite Rotor Blade Cross-Sectional Modeling," *Journal of the American Helicopter Society*, Vol. 42, No. 1, 1997, pp. 27–38.

[10]Palacios, R. and Cesnik, C. E. S., "Cross-Sectional Analysis of Non-Homogeneous Anisotropic Active Slender Structures," *AIAA Journal*, Vol. 43, No. 12, 2005, pp. 2624–2638.

[11]Anderson, W. K. and Bonhaus, D. L., "An Implicit Upwind Algorithm for Computing Turbulent Flows on Unstructured Grids," *Computers & Fluids*, Vol. 23, No. 1, 1994, pp. 1–21.

[12]NASA LaRC, Hampton, VA, *FUN3D 12.2-63280 Manual*, Nov. 2012, http://fun3d.larc.nasa.gov.

[13]Kreshock, A. R., *Design, Analysis and Testing of Active Twist Rotor Blades*, Master's thesis, Old Dominion University, Norfolk, VA, 2013.

[14]Biedron, R. T. and Lee-Rausch, E. M., "Computation of UH-60A Airloads Using CFD/CSD Coupling On Unstructured Meshes," *American Helicopter Society 67th Annual Forum Proceedings*, Virginia Beach, VA, May 2011.

[15]Yeager, W. T., Wilbur, M. L., and Nixon, M. W., "A Review of Recent Rotorcraft Investigations in the Langley Transonic Dynamics Tunnel," AIAA Paper 2003-1963, 2003.

[16]Pirzadeh, S. Z., "Advanced Unstructured Grid Generation for Complex Aerodynamic Applications," AIAA Paper 2008–7178, Aug. 2008.

[17]Samareh, J. A., "Unstructured Grids on NURBS Surfaces," AIAA Paper 1993–3454, 1993.

[18]Biedron, R. T. and Lee-Rausch, E. M., "Rotor Airloads Prediction Using Unstructured Meshes and Loose CFD/CSD Coupling," AIAA Paper 2008-7341, 2008.

[19]Spalart, P. R. and Allmaras, S. R., "A One-Equation Turbulence Model for Aerodynamic Flows," *La Recherche Aerospatiale*, No. 1, 1994, pp. 5–21.

[20]Roe, P. L., "Approximate Riemann Solvers, Parameter Vectors, and Difference Schemes," *Journal of Computational Physics*, Vol. 43, 1981, pp. 357–372.

[21]Nyukhtikov, M., Smelova, N., Mitchell, B. E., and Holmes, D. G., "Optimized Dual-Time Stepping Technique For Time-Accurate Navier-Stokes Calculation," *Proceedings of the 10th International Symposium on Unsteady Aerodynamics, Aeroacoustics and Aeroelasticity of Turbomachines*, 2003.

[22]Vatsa, V. N., Carpenter, M. H., and Lockard, D. P., "Re-evaluation of an Optimized Second Order Backward Difference (BDF2OPT) Scheme for Unsteady Flow Applications," AIAA Paper 2010–0122, Jan. 2010.

[23]Thomas, P. D. and Lombard, C. K., "Geometrical Conservation Law and Its Application," *AIAA Journal*, Vol. 17, No. 10, Oct. 1978, pp. 1030–1037.

[24]Noack, R. W., "DiRTlib: A Library to Add an Overset Capability to Your Flow Solver," AIAA Paper 2005-5116, June 2005.

[25]Noack, R. W., "SUGGAR: a General Capability for Moving Body Overset Grid Assembly," AIAA Paper 2005-5117, June 2005.

[26]Tung, C., Caradonna, F., and Johnson, W., "The Prediction of Transonic Flows on an Advancing Rotor," *American Helicopter Society 40th Annual Forum Proceedings*, Arlington, VA, May 1984.

Figure 1. ARES/ATR model in the Transonic Dynamics Tunnel.

American Institute of Aeronautics and Astronautics

Figure 2. ATR blade shown with piezoelectric actuators.
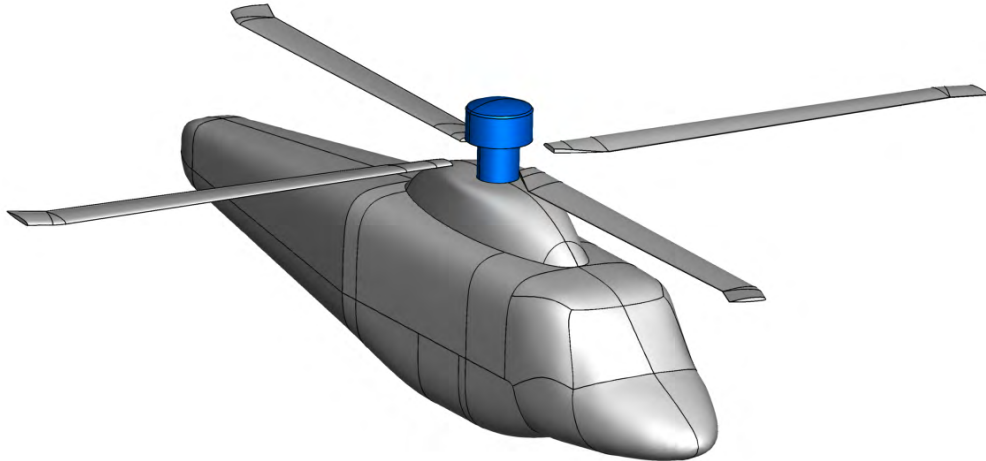
Figure 3. Surface definition of ARES/ATR CFD model. Mast and hub cover shown in blue.

y^+:   0 0.2 0.4 0.6 0.8 1 1.2 1.4 1.6 1.8 2
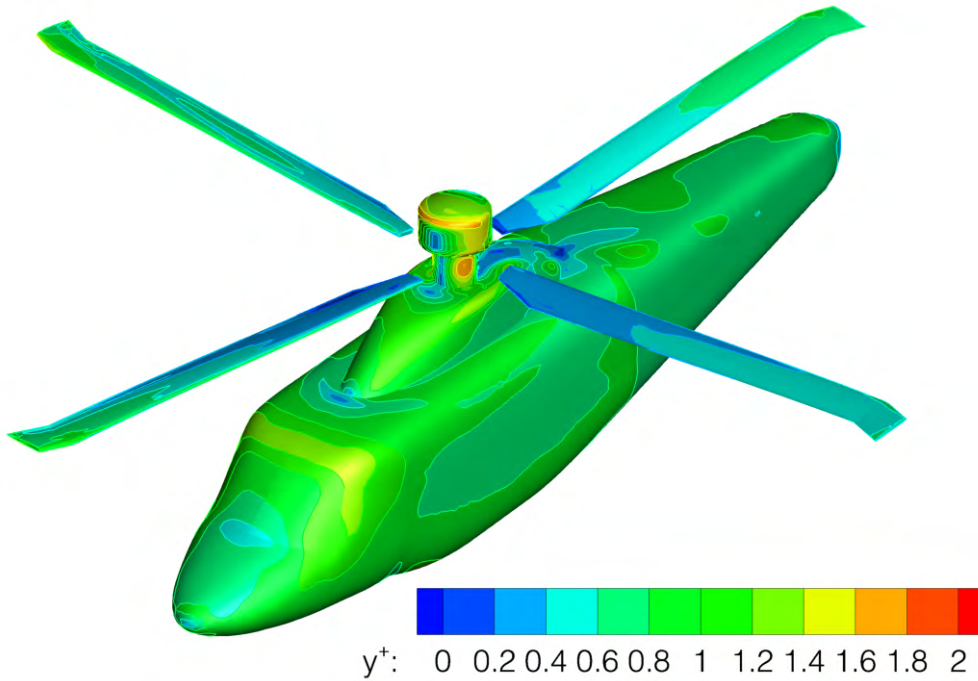
Figure 4. Contours of y^+ on the fine mesh at advance ratio 0.4 conditions.

American Institute of Aeronautics and Astronautics
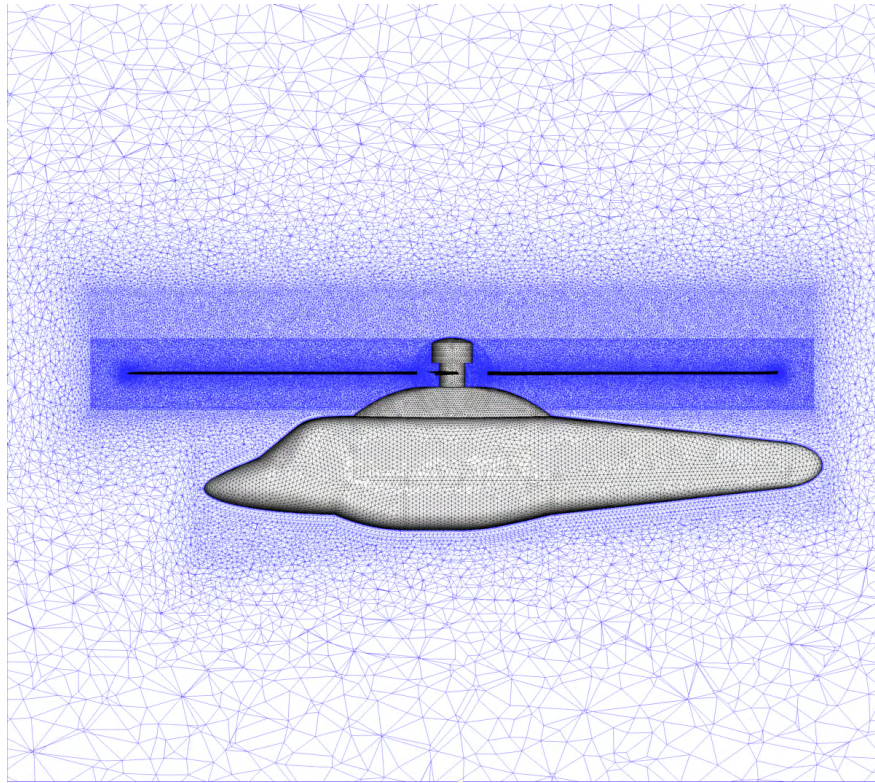
Figure 5. Surface mesh in black with a centerline plane cut in blue for the medium mesh.
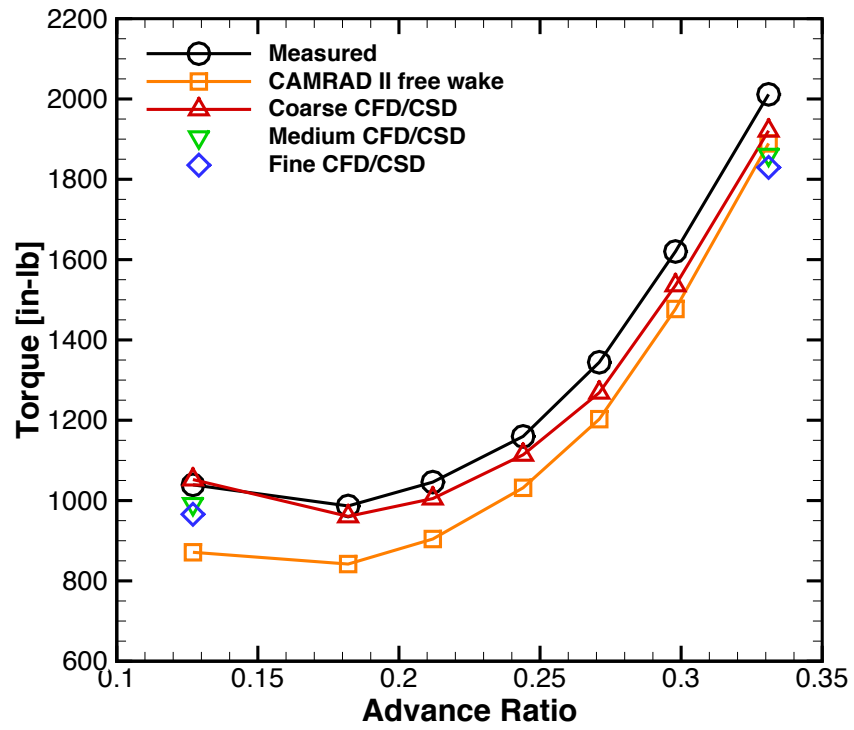
Figure 6. Computed and measured rotor torque.
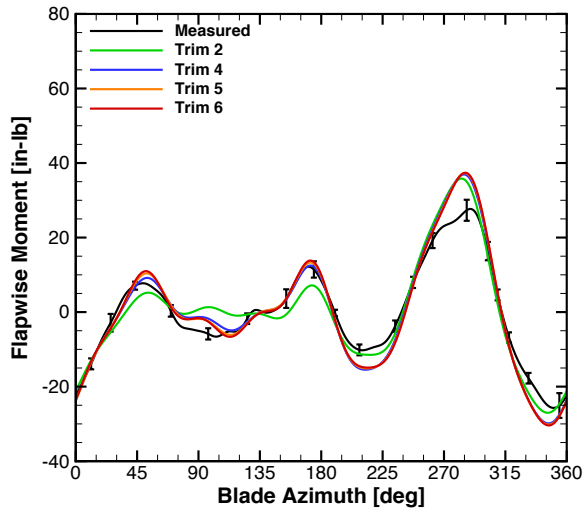
American Institute of Aeronautics and Astronautics
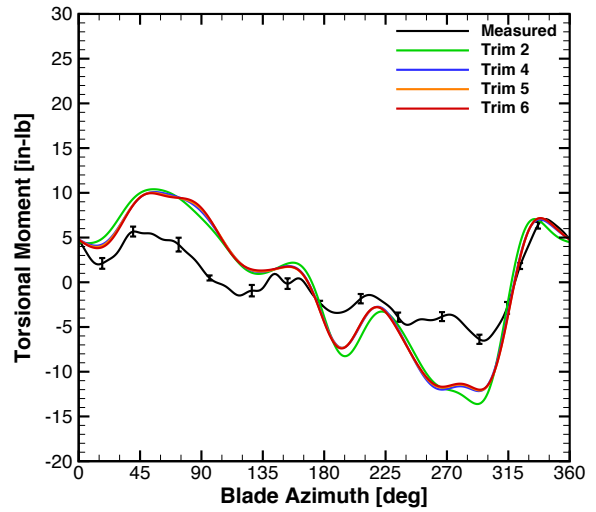
(a) Flapwise bending moment (mean removed) at $R = 0.76$.

(b) Torsional bending moment (mean removed) at $R = 0.24$.
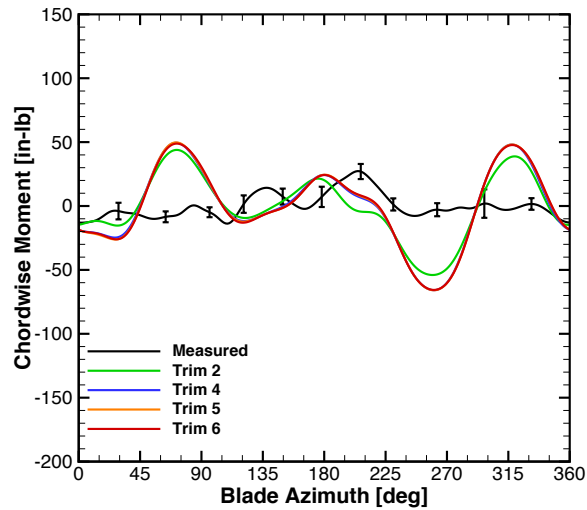
(c) Chordwise bending moment (mean removed) at $R = 0.20$.

Figure 7. **CFD/CSD trim convergence for fine mesh for $\mu = 0.13$.**
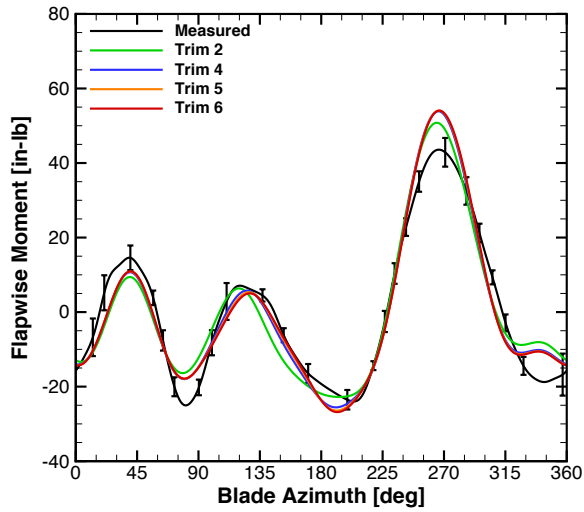
(a) Flapwise bending moment (mean removed) at $R = 0.76$.
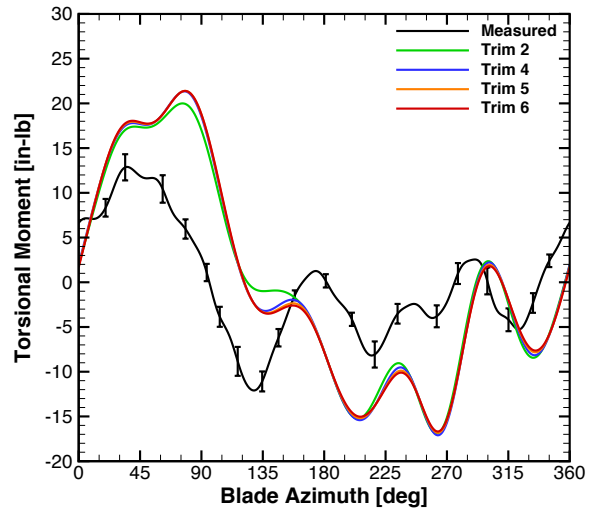
(b) Torsional bending moment (mean removed) at $R = 0.24$.
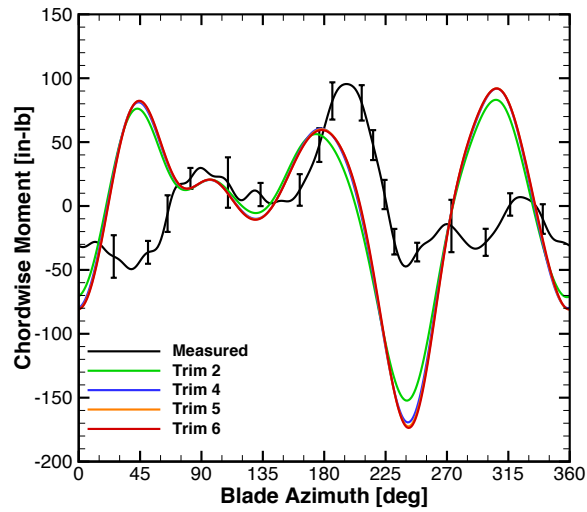
(c) Chordwise bending moment (mean removed) at $R = 0.20$.

Figure 8. CFD/CSD trim convergence for fine mesh for $\mu = 0.33$.
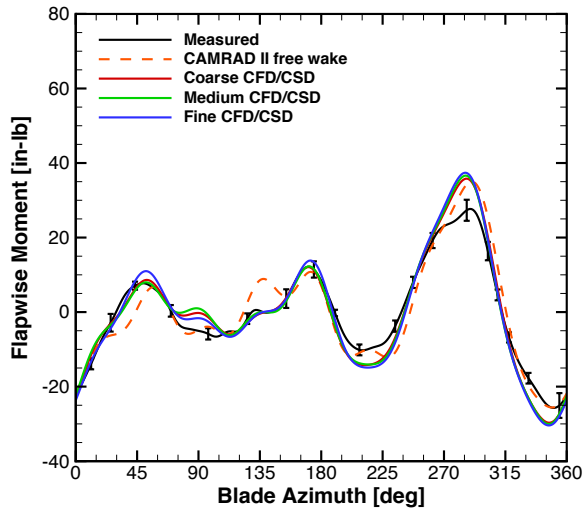
(a) Flapwise bending moment (mean removed) at $R = 0.76$.
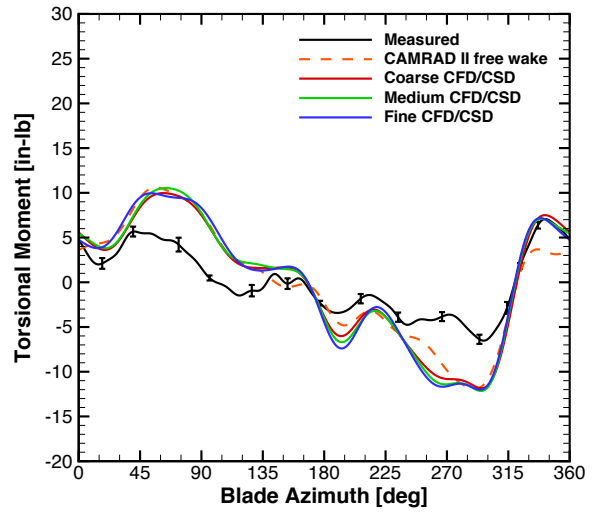
(b) Torsional bending moment (mean removed) at $R = 0.24$.
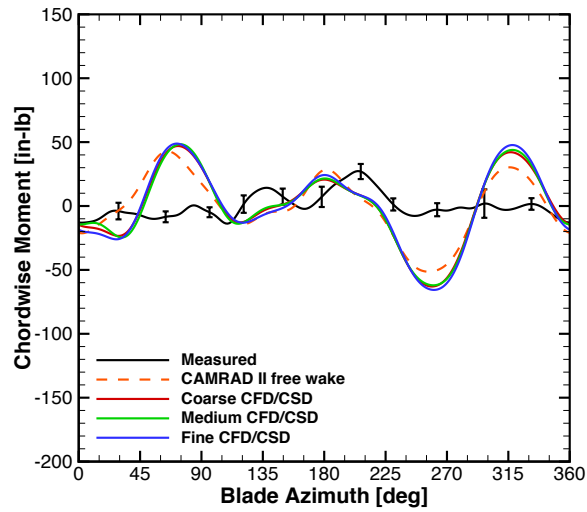
(c) Chordwise bending moment (mean removed) at $R = 0.20$.

Figure 9. Airload mesh convergence for $\mu = 0.13$.
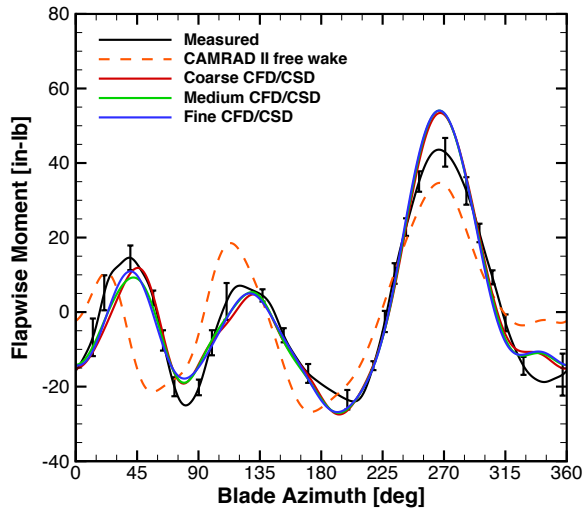
(a) Flapwise bending moment (mean removed) at $R = 0.76$.
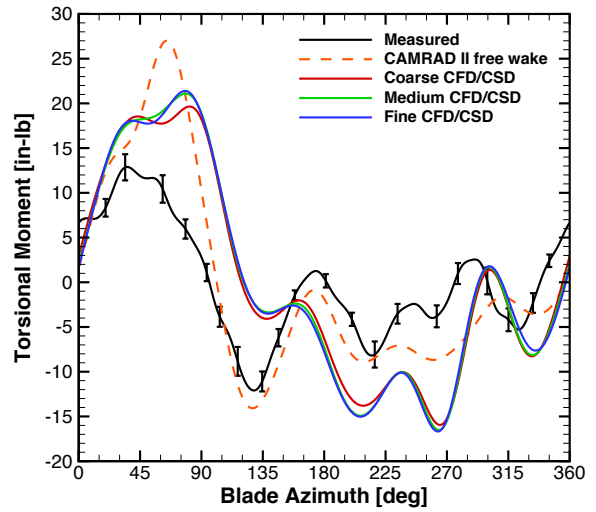
(b) Torsional bending moment (mean removed) at $R = 0.24$.
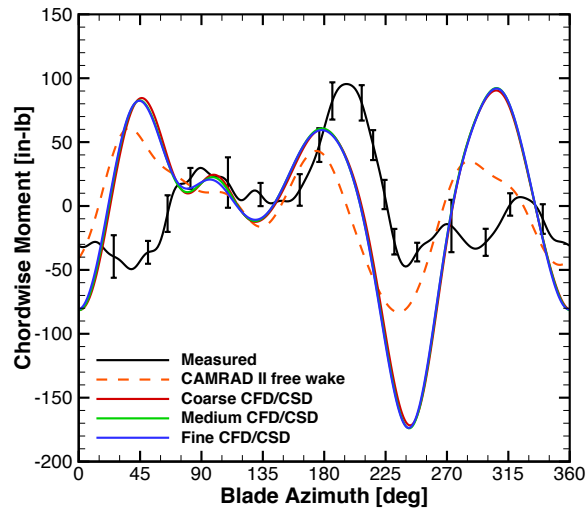
(c) Chordwise bending moment (mean removed) at $R = 0.20$.

Figure 10. Airload mesh convergence for $\mu = 0.33$.
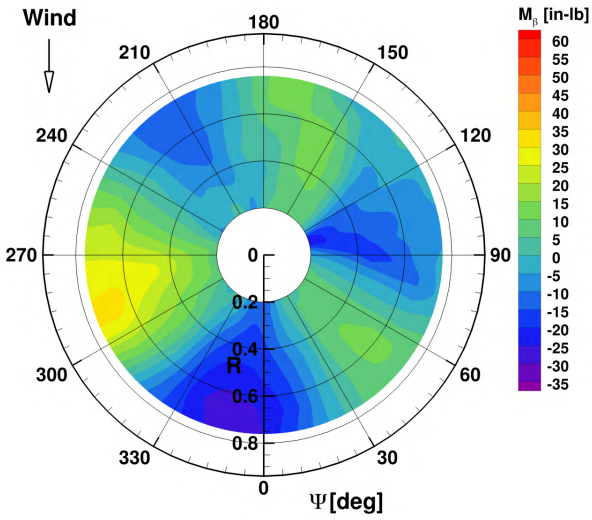
(a) Blade 1
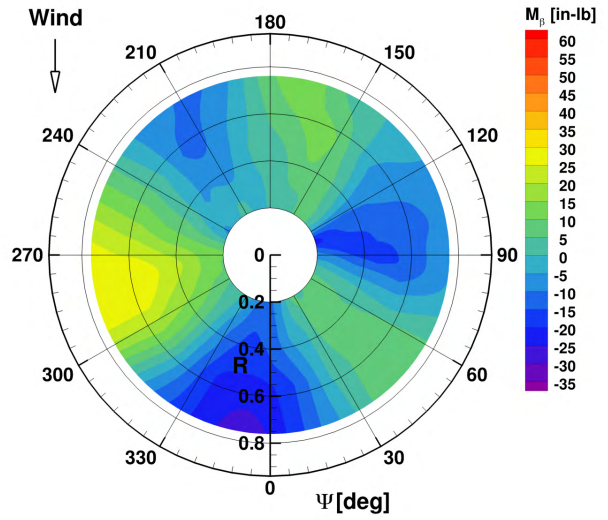
(b) Blade 2
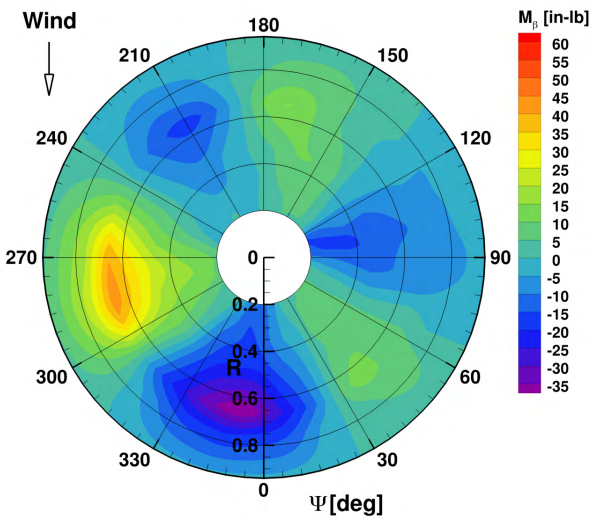
(c) Blade 3
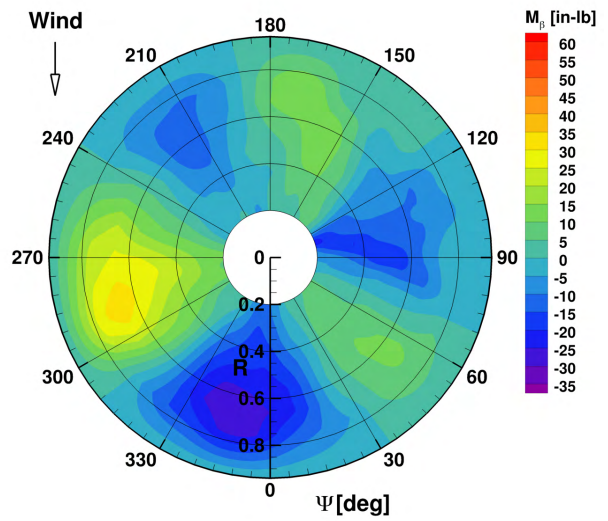
(d) Blade 4

Figure 11. Flapwise bending moment (mean removed) for each blade for $\mu = 0.13$.

American Institute of Aeronautics and Astronautics
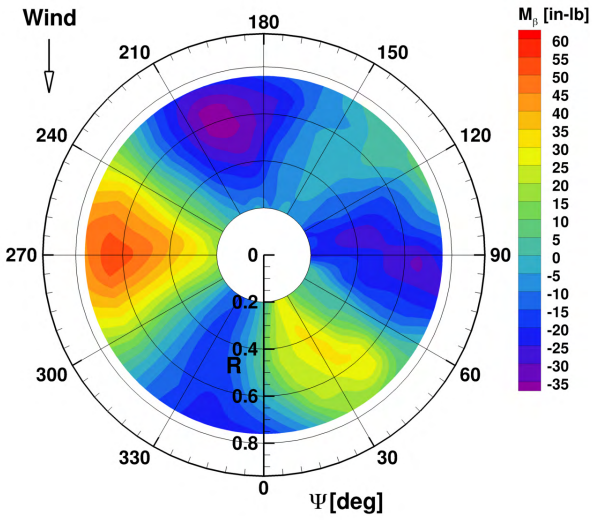
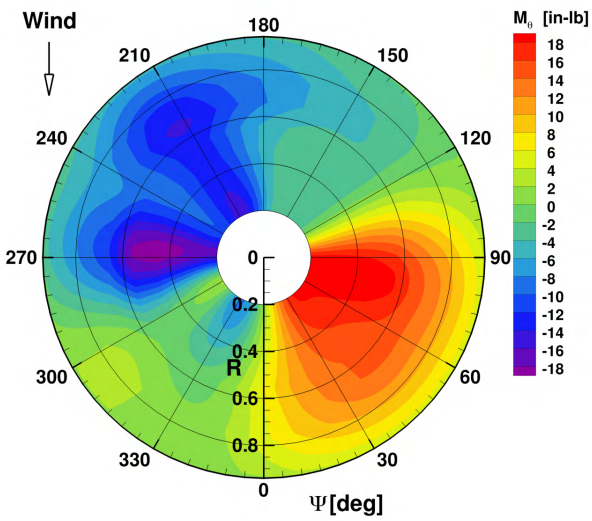(a) Blade 1
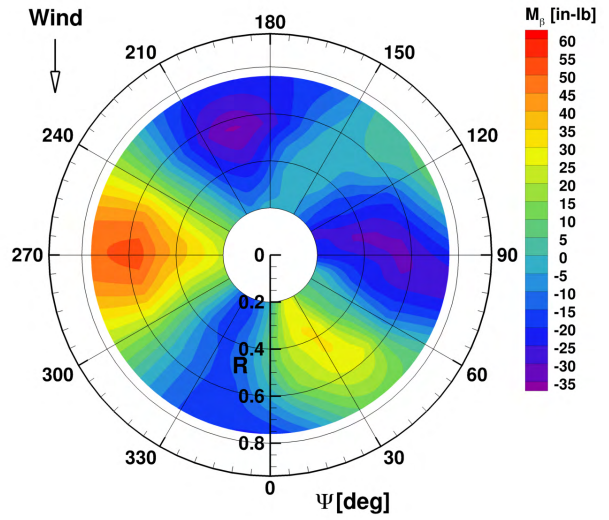
(b) Blade 2
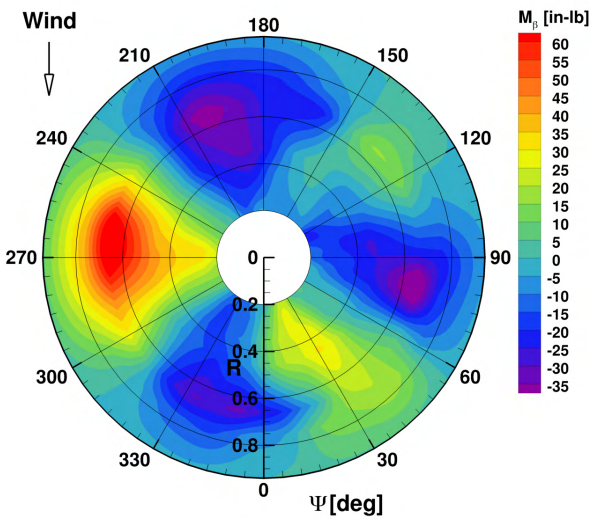
(c) Blade 3
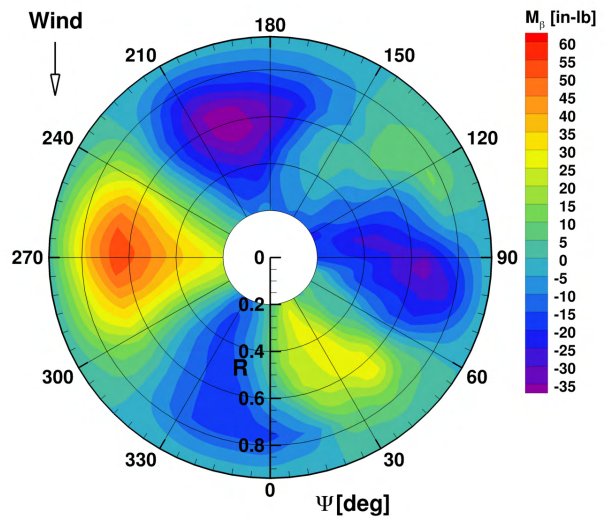
(d) Blade 4

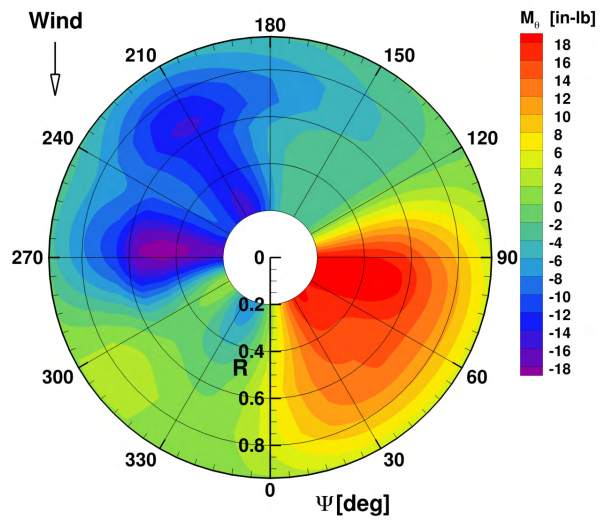Figure 12. Flapwise bending moment (mean removed) for each blade for $\mu = 0.33$.
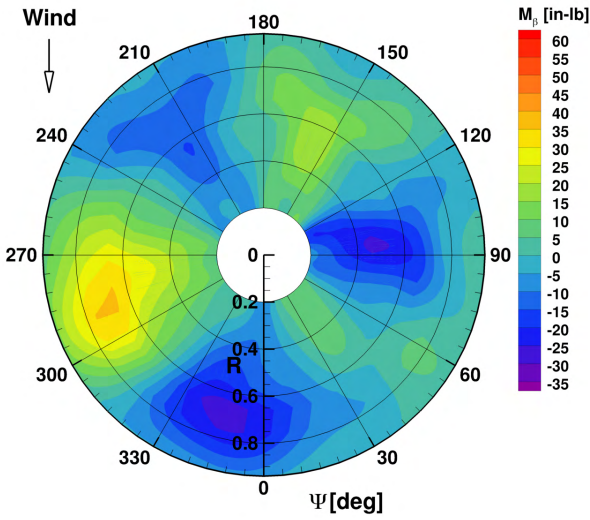
(a) CAMRAD II free wake
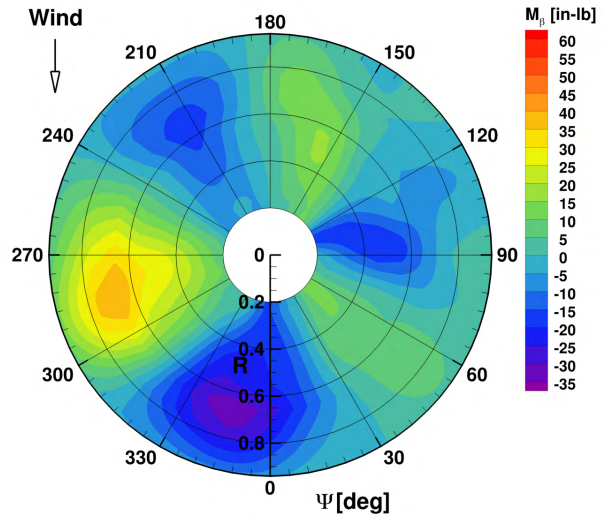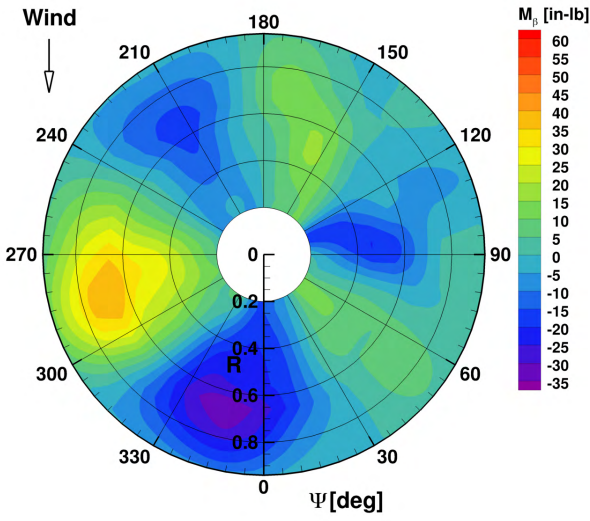
(b) Coarse CFD/CSD
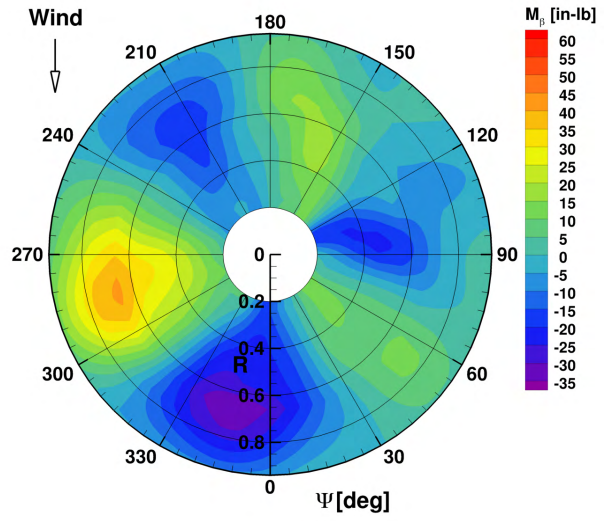
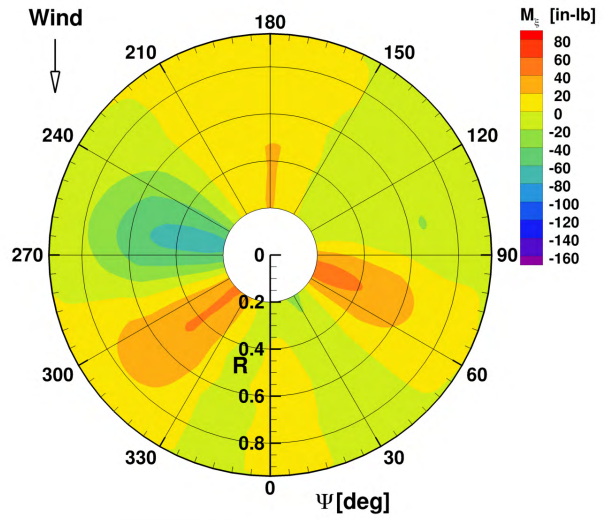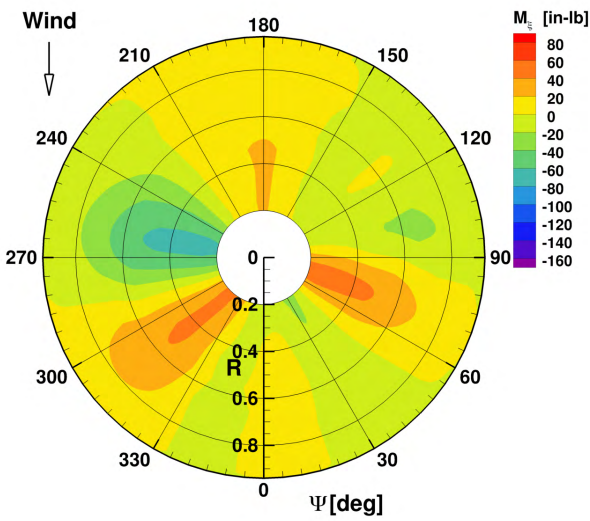(c) Medium CFD/CSD
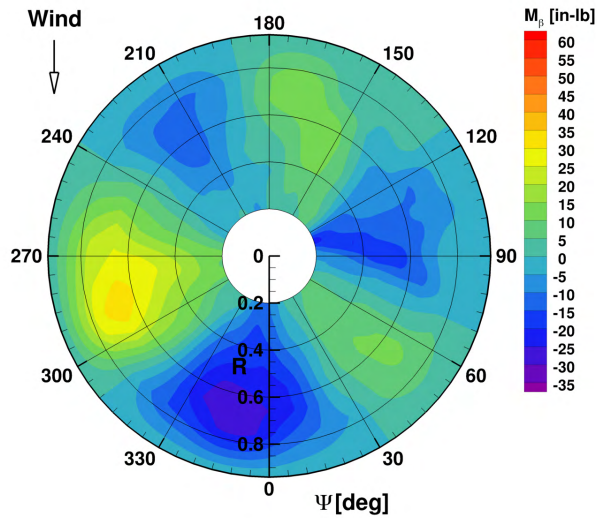
(d) Fine CFD/CSD

(e) Measured (Blade 4)

Figure 13. Flapwise bending moment (mean removed) mesh convergence for $\mu = 0.13$.
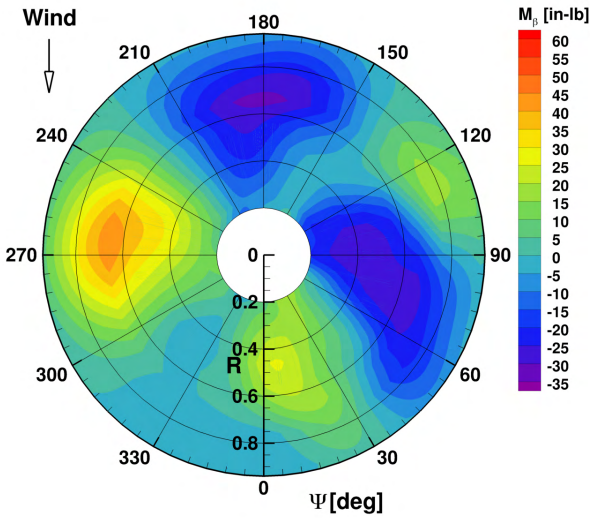
American Institute of Aeronautics and Astronautics

(a) CAMRAD II free wake
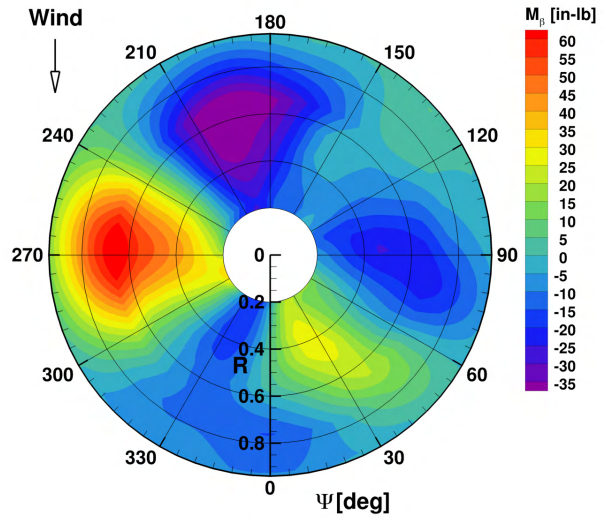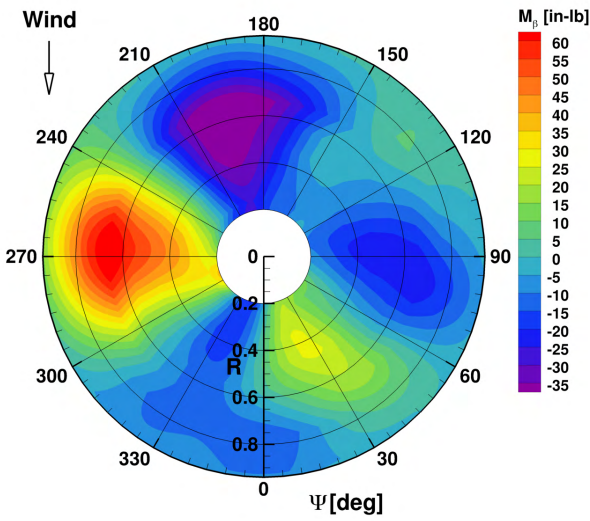
(b) Coarse CFD/CSD
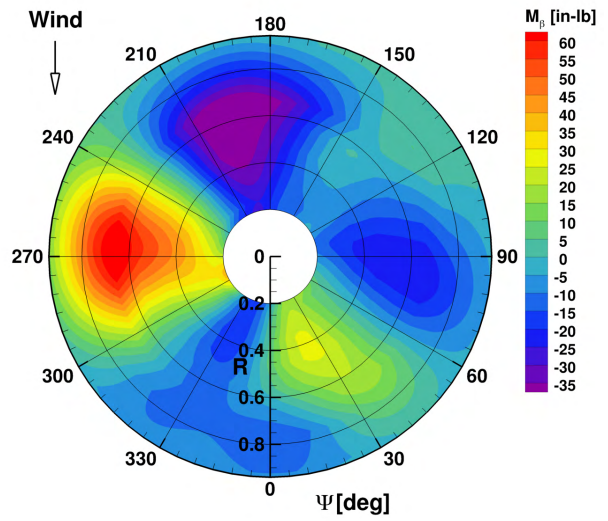
(c) Medium CFD/CSD
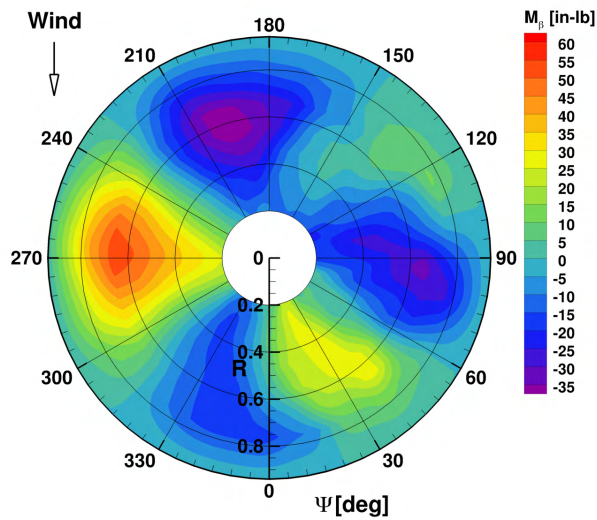
(d) Fine CFD/CSD

(e) Measured (Blade 4)

Figure 14. Flapwise bending moment (mean removed) mesh convergence for $\mu = 0.33$.

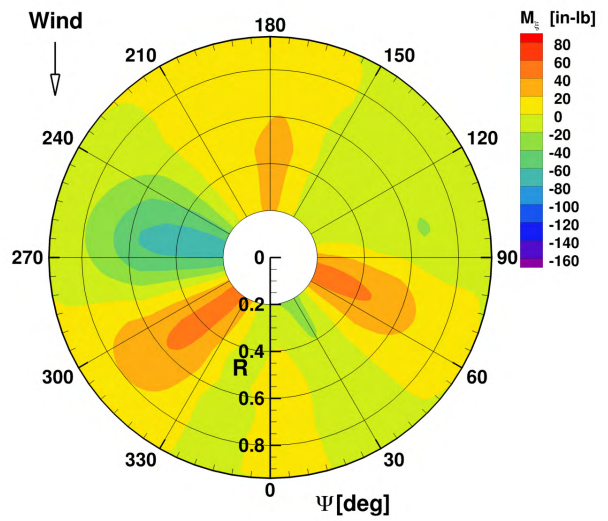American Institute of Aeronautics and Astronautics
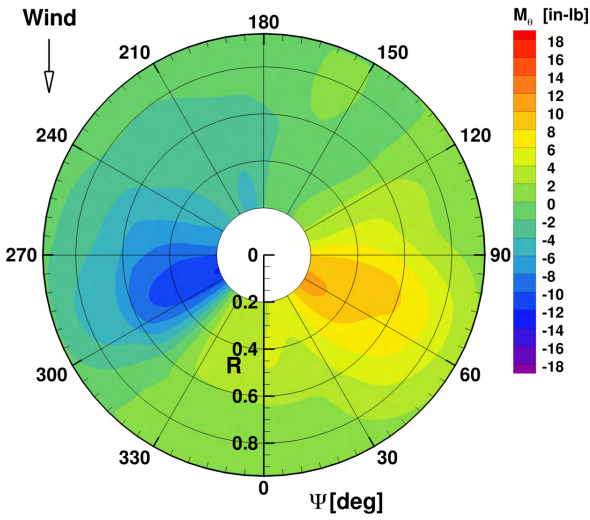
(a) CAMRAD II free wake

(b) Coarse CFD/CSD

(c) Medium CFD/CSD

(d) Fine CFD/CSD

Figure 15. Torsional bending moment (mean removed) mesh convergence for $\mu = 0.13$.

American Institute of Aeronautics and Astronautics
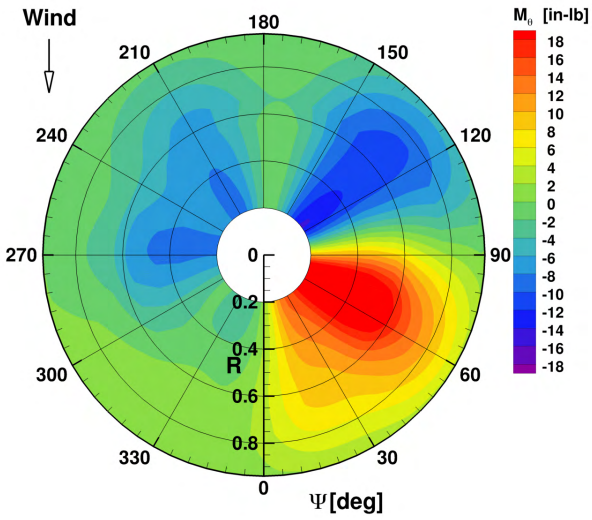
(a) CAMRAD II free wake
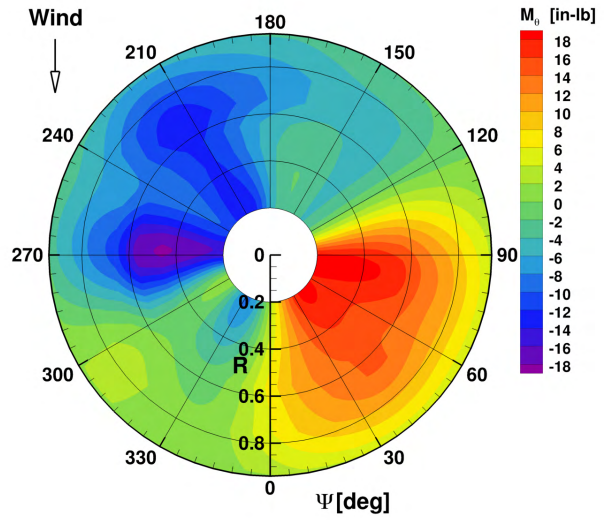
(b) Coarse CFD/CSD

(c) Medium CFD/CSD

(d) Fine CFD/CSD

Figure 16. **Torsional bending moment (mean removed) mesh convergence for** $\mu = 0.33$**.**

American Institute of Aeronautics and Astronautics
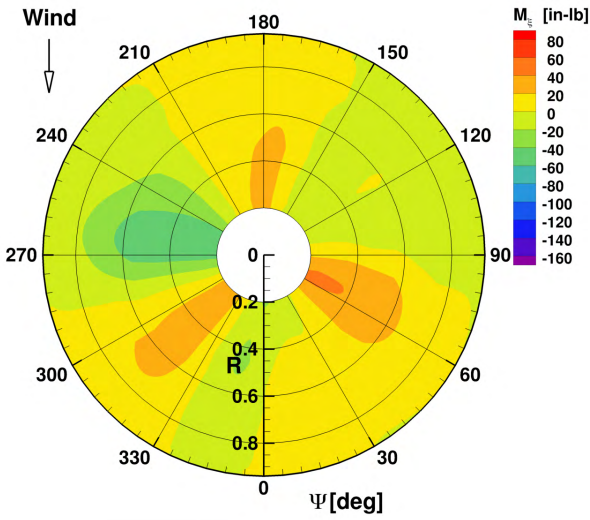
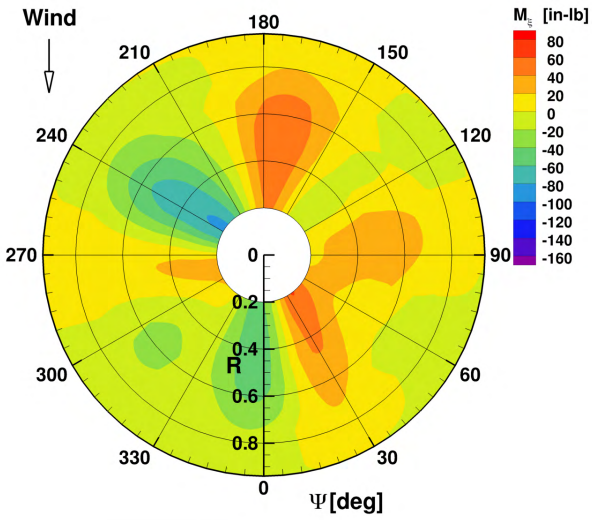(a) CAMRAD II free wake

(b) Coarse CFD/CSD

(c) Medium CFD/CSD

(d) Fine CFD/CSD

Figure 17. Chordwise bending moment (mean removed) mesh convergence for $\mu = 0.13$.
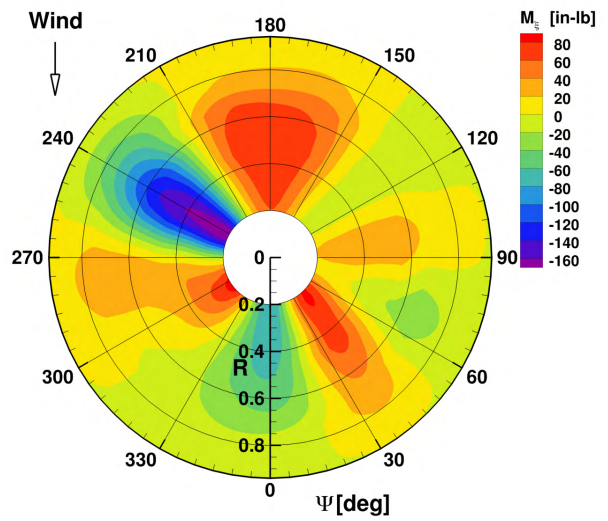
American Institute of Aeronautics and Astronautics

(a) CAMRAD II free wake
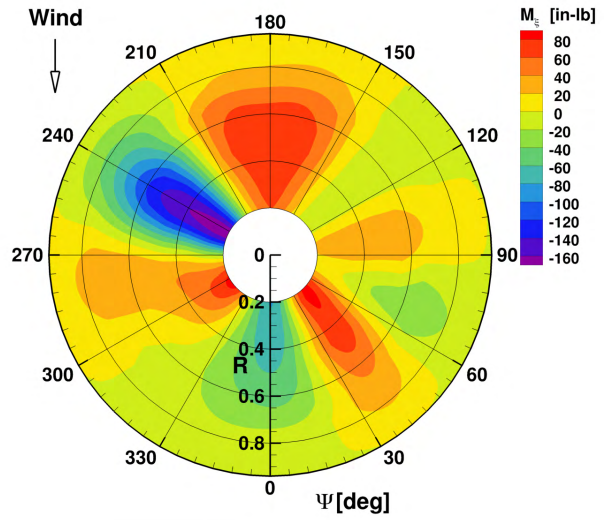
(b) Coarse CFD/CSD
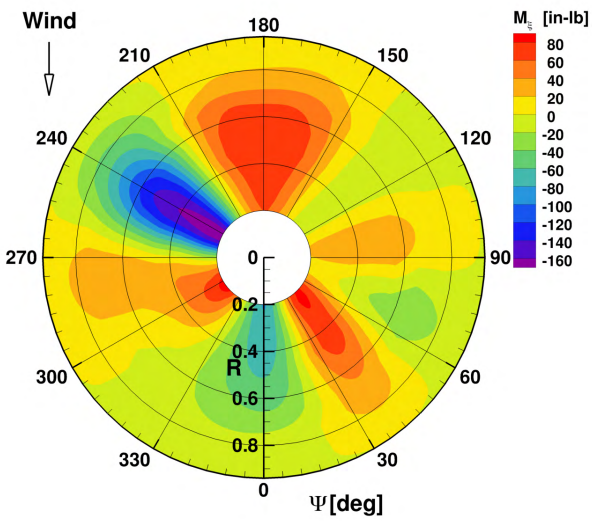
(c) Medium CFD/CSD

(d) Fine CFD/CSD

Figure 18. Chordwise bending moment (mean removed) mesh convergence for $\mu = 0.33$.

American Institute of Aeronautics and Astronautics